Acta Materialia 244 (2023) 118593

Contents lists available at ScienceDirect

Acta Materialia

journal homepage: www.elsevier.com/locate/actamat

Flash sintering with concurrent crystallization of $Li_{1.5}Al_{0.5}Ge_{1.5}(PO_4)_3$ glass

João V. Campos [a,b,c,*], Isabela R. Lavagnini [d,e], Vinicius M. Zallocco [a,b,c], Eduardo B. Ferreira [c,f], Eliria M.J.A. Pallone [d,e], Ana C.M. Rodrigues [b,c]

[a] Materials Science and Engineering Graduate Program, Federal University of São Carlos, 13565-905 São Carlos, SP, Brazil
[b] Department of Materials Engineering, Federal University of São Carlos, 13635-905 São Carlos, SP, Brazil
[c] Center for Research, Technology and Education of Vitreous Materials, CeRTEV – FAPESP, LaMaV, DEMa/UFSCar, 13565-905 São Carlos, SP, Brazil
[d] Department of Biosystem Engineering, University of São Paulo, USP, Av. Duque de Caxias Norte, 225, 13635-900 Pirassununga, SP, Brazil
[e] Materials Science and Engineering Graduate Program, University of São Paulo, USP/FZEA, Av. Duque de Caxias Norte, 225, 13635-900 Pirassununga, Brazil
[f] Department of Materials Engineering, São Carlos School of Engineering, University of São Paulo USP, 13566-590 São Carlos, SP, Brazil

ARTICLE INFO

Keywords:
LAGP
NaSICON
Solid-state electrolyte
Reactive flash sintering
Glass-ceramic

ABSTRACT

Single-phase $Li_{1.5}Al_{0.5}Ge_{1.5}(PO_4)_3$ NaSICON (Na superionic conductor) glass-ceramic is obtained via a new route using *flash-sinter crystallization*. Green compacts of glass powder are sinter-crystallized in a few seconds. The results suggest that controlling the current increase during the flash event is needed to avoid overheating, which could cause the melting of the samples. A processing map for the flash sinter-crystallization of $Li_{1.5}Al_{0.5}Ge_{1.5}(PO_4)_3$ is developed and presented based on the current density and holding time at the steady state. The samples fabricated by flash sinter-crystallization are compared with those conventionally heated. Using this novel technique, single-phase glass-ceramics are obtained with total ionic conductivity at room temperature surpassing that of glass-ceramics prepared by conventional heating (2.26 10^{-4} S cm^{-1} and 1.36 10^{-4} S cm^{-1}, respectively).

1. Introduction

Because of the increased demand for high-energy-density batteries led by the electric-vehicle industry, safer options for lithium-ion batteries are being extensively studied. In this context, the all-solid-state lithium battery (ASSB) is a promising technology that uses inorganic ceramics as a fast lithium-ion conductor to replace flammable liquid electrolytes, improving safety and increasing energy density [1–4]. Solid superionic conductors, such as lithium-NaSICON $Li_{x+1}Al_xGe_{x+1}(PO_4)_3$ (LAGP) and $Li_{x+1}Al_xTi_{x+1}(PO_4)_3$ (LATP), have been investigated because of their high ionic conductivity at room temperature (1–10 mS cm^{-1}) and stability [5]. LAGP has been synthesized by different methods so far [6,7], e.g., solid-state reaction [8], Pechini [9], sol-gel [10], co-precipitation/freeze drying [11], and glass-ceramics from the melting-quenching and crystallization route [12–15].

The glass-ceramic route involves controlling the crystallization of a precursor glass under different heat treatment conditions. The possibility of designing the microstructure in terms of grain size, crystalline phase fraction, and porosity is an advantage of this method [16,17]. However, glass crystallization at high temperatures can take several hours (e.g., Fu [15] crystallized a LAGP glass at 622 °C for 12 h), which can be a drawback for manufacturing materials containing highly volatile components, such as LAGP.

As a new alternative to ceramic processing, flash sintering has been drawing the scientific community's attention for being a faster and more energy-efficient method than conventional sintering [18]. For instance, several ceramics were fully densified in a few seconds using flash sintering at a furnace temperature considerably lower than the one needed in conventional sintering [19–22]. This technique applies an electric field directly to the sample during heating using two metallic electrodes. Then, in a critical combination of electric field and temperature, a thermal runaway event occurs, rapidly raising the electric current passing through the sample and heating it from the inside out extremely fast (in the order of 10^4 °C min^{-1}) [23,24]. To control the maximum temperature reached by the sample during the thermal runaway, it is possible to monitor the power supply that applies the electric field and switch to a current-control mode, thus controlling the current limit.

Since the seminal work of Cologna et al. in 2010 [18], several new approaches to flash sintering have emerged. For instance, Current Ramp Flash Sintering (CRFS) is a method that controls the current density at a

* Corresponding author.
E-mail address: joao.campos@ufscar.br (J.V. Campos).

https://doi.org/10.1016/j.actamat.2022.118593
Received 30 May 2022; Received in revised form 23 November 2022; Accepted 4 December 2022
Available online 5 December 2022
1359-6454/© 2022 Acta Materialia Inc. Published by Elsevier Ltd. All rights reserved.

constant rate to avoid power overshoot during the flash event (thermal runaway onset) [24–26]. New possibilities for flash-like experiments have also emerged, for example, Flash Synthesis [27,28] and Reactive Flash Sintering (RFS) [29–35]. Flash Synthesis uses the thermal runaway and athermal effects of the flash event to accelerate material synthesis at low furnace temperatures. The RFS approach combines Flash Synthesis with sintering in a single step.

The starting material used in RFS experiments includes crystalline precursor powders mixed at the desired stoichiometry [29,36] or amorphous precursor powders obtained by a chemical synthesis method [27,30] to synthesize a material with the desired phases by solid-state reaction.

Here, we propose using a new variant of flash sintering to combine the grain-size control of the glass-ceramics route with the rapid processing time of flash sintering. We named this new variant *'Flash Sinter–Crystallization'* (FSC), in which sintering with concurrent crystallization of the glass phase is achieved. It is worth mentioning that conventional flash-like experiments have already been successfully applied in glass systems [37–41] and glass-ceramics [42] but without crystallization during the flash event. Thus, to our knowledge, this is the first scientific paper to report glass crystallization using a flash-like experiment. Yoon et al. [35] recently published a comprehensive review on reactive flash sintering in which they pointed out that the flash event has not yet been used to crystallize glass and would be of great interest in this field.

In this context, we hypothesize that the rapid heating rate of the flash event and athermal effects caused by the electric field would prevent the loss of volatile compounds and promote rapid sinter-crystallization of the LAGP NaSICON phase starting from an isochemical precursor glass. The *FSC* variant approach is expected to favor crystal growth, improving the material's ionic conductivity.

2. Material and methods

2.1. Synthesis of the precursor glass

$Li_{1.5}Al_{0.5}Ge_{1.5}(PO_4)_3$ (LAGP) precursor glass with composition 0.1875 Li_2O - 0.0625 Al_2O_3 - 0.375 GeO_2 - 0.375 P_2O_5 plus 5 mol% Li_2O excess [43] was prepared using commercial reagent-grade Li_2CO_3 (Dinâmica, 99.85%), Al_2O_3 (Sigma-Aldrich, 99.90%), GeO_2 (Alfa Aesar, 99.99%), and $(NH_4)_2HPO_4$ (Sigma-Aldrich, 98.00%) powders. The reagents were dried at 120 °C for 24 h and then ground in a ball mill in a dry condition in a polyethylene jar using alumina grinding balls for 10 h. Next, the resulting mixture was heated (10 °C min^{-1} heating rate) in an alumina crucible up to 700 °C for 1 h to decompose Li_2CO_3 and $(NH_4)_2HPO_4$, releasing NH_3, CO_2, and H_2O. Finally, the mixture was melted at 1250 °C for 30 min (10 °C min^{-1}), and the molten material was poured and pressed between two stainless steel plates (splat-cooling), forming a ~1 mm thick glass plate. In a previous work [13], the chemical composition of a LAGP glass prepared in the same way was determined by inductively coupled plasma optical emission (ICP-OES). No significant lithium volatilization was identified in their case. Therefore, it is reasonable to admit that the desired stoichiometry has not changed significantly during the melting process in the present work.

A small fragment of the precursor glass was used to determine the glass transition (T_g) and crystallization (T_x) temperatures using differential scanning calorimetry (DSC: 404, Netzsch) in the room atmosphere. The DSC analysis was performed in a platinum crucible using a heating rate of 10 °C min^{-1}.

The precursor glass was crushed using an agate mortar and pestle. The resulting glass powder was dry milled in a polyethylene jar using alumina grinding balls for 24 h and then sieved through an 80-mesh sieve. Cylindrical glass powder compacts with 4.3 mm in height and 6.2 mm in diameter were formed by uniaxial pressing (250 MPa). A silver paste was applied onto both flat surfaces of the pellets to improve their electrical contact and allow the reversible electrochemical reaction between the ionic conductor (LAGP) and the electrodes (electronic conductors), as previously reported by Caliman et al. [44] and Lachal et al. [45].

2.2. Heat treatment & characterization

LAGP samples were sintered and concurrently crystallized for the first time by flash sintering. To this end, a setup described in detail in a previous work [46] was used. The electric field used in all experiments was AC 1000 Hz (sinusoidal wave), with a magnitude of 150 V cm^{-1} (RMS values), which was turned on from the beginning of the furnace heating. The furnace temperature was set to reach 500 °C (20 °C min^{-1} heating rate) and was kept at this level until the end of the experiment, i.e. when the power supply was turned off. We varied the maximum current density from 10 to 100 mA mm^{-2} (with 10 mA mm^{-2} increments) and the holding time (the time the power supply was kept on after reaching the maximum current density) from 20 s to 120 min (20 s, 30 min, and 120 min). The current increase was controlled as a ramp with a slope of 0.5 mA mm^{-2} s^{-1} using CRFS [24,25,47,48] to avoid overheating during the flash event (when the power supply starts to operate in the current-control mode). The samples were labeled according to the employed current density (J in mA mm^{-2}), sintering method, and holding time (t in minutes) – $^{\#t}CRFS_{\#J}$, e.g., the sample subjected to 20 mA mm^{-2} for 120 min was labeled $^{120}CRFS_{20}$.

Furthermore, a traditional flash sintering experiment was performed (without controlling the current ramp during the flash event). In this case, a current density of 40 mA mm^{-2} and a holding time of 1 min were used. Both experiments were carried out at a constant heating rate, i.e., the power supply was turned on at the beginning of the furnace heating. The furnace was set to heat up to 500 °C at a rate of 20 °C min^{-1}.

One specimen (sample labeled CS) was conventionally sintered. This sample was heated up to 850 °C at a rate of 10 °C min^{-1} with a holding time of 12 h. Table S1 in the Supplementary Material presents all the experimental conditions and their respective labels.

A thermocouple was placed 10 mm away from the sample during flash sintering to measure the furnace temperature (T_f). The black-body radiation (BBR) model was used to estimate the actual sample surface temperature, considering the Joule heating process during flash sintering [26,49]:

$$mC_p\frac{dT_s}{dt} = VI - \sigma_{SB}\varepsilon A\left(T_s^4 - T_f^4\right), \quad (1)$$

where m is the sample mass (kg), C_p is the sample heat capacity at constant pressure(calculated for each temperature using the polynomial equation proposed by Rohde et al. [50]), t is the time (s), V is the RMS magnitude of the voltage (V), I is the RMS magnitude of the current (A), σ_{SB} is the Stefan-Boltzmann constant (5.67 10^{-8} W m^{-2} K^{-4}), ε is the sample emissivity (assumed as 0.8), and A is the sample surface area (radial and flat surfaces of the cylinder) (m^2). The specimen can experience a thermal gradient during flash sintering [51,52]; however, for the sake of simplicity, it was assumed that the whole sample was at the same temperature (T_s) for each instant of time.

X-ray diffraction (XRD) was used to analyze the crystalline phases, crystallinity, and crystallite sizes of the samples. XRD analyses were carried out using Cu-K_α radiation (Rigaku Miniflex 600) in a 2θ range of 10–60° and a step width of 0.02° at a scan speed of 2° min^{-1}. The crystalline phases and crystallite sizes were determined by Rietveld refinement using the GSAS-II software [53]. The flat surfaces of the flash sinter-crystallized samples were analyzed by XRD. The flat surfaces were gently polished with a 600-grit diamond disk before analysis to remove the silver paste. Likewise, the diffractogram of the LAGP glass (before *FSC*) was also obtained.

The green density values of the pressed compacts were calculated from their mass and geometry, measuring their thickness and diameter

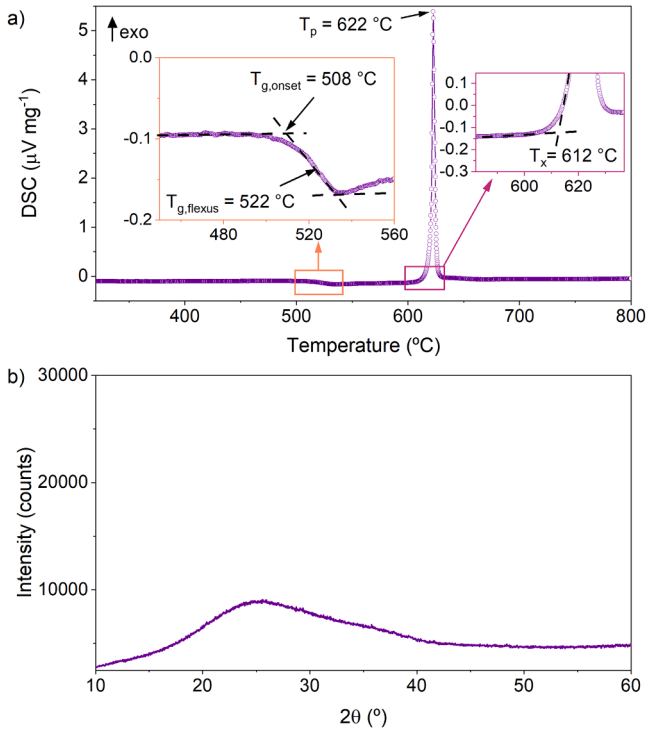

Fig. 1. (a) DSC (10 °C min^{-1} heating rate in the room atmosphere) pattern and (b) X-ray diffractogram of the $Li_{1.5}Al_{0.5}Ge_{1.5}(PO_4)_3$ glass. The glass transition ($T_{g,onset}$ and $T_{g,flexus}$), the crystallization peak temperature (T_p), and the onset of crystallization (T_x) are shown in a).

using a caliper and determining the mass/volume of the cylinder. After sinter-crystallization, all specimens had their apparent density calculated by the Archimedes principle. Their masses were measured dry, immersed, and soaked in distilled water on a laboratory scale (Mettler Toledo lab balance). The theoretical density of the LAGP crystalline phase was estimated from the Rietveld refinement of the x-ray diffractograms as 3.56 g cm^{-3}.

Scanning electron microscopy (SEM) and energy dispersive spectroscopy (EDS) were performed on a fracture surface of the sintered compacts using a scanning electron microscope with field emission gun FEG-SEM XL30 (Phillips Electron Optics BV) coupled to an energy dispersive X-ray (EDX) source. After diametrically fracturing the cylindrical samples, a thin gold layer was deposited on the fractured surfaces for SEM analyses (Quorum Q150R ES equipment).

The electrical conductivity of the sinter-crystallized specimens as a function of frequency and temperature was determined by electrochemical impedance spectroscopy (EIS). Both flat surfaces of the specimens were polished and sputtered with gold (Quorum Q150R ES equipment), making them into electrodes. We varied the frequency from 10 MHz to 10 Hz and the temperature from 30 to 170 °C (eight temperature levels equally spaced). The applied voltage for the EIS measurements was 300 mV.

3. Results and discussion

Fig. 1a shows the DSC curves of the precursor glass (0.1875 Li_2O - 0.0625 Al_2O_3 - 0.375 GeO_2 - 0.375 P_2O_5), evidencing the regions (figure insets) where the glass transition temperature ($T_{g,onset}$ = 508 °C; $T_{g,flexus}$ = 522 °C), the crystallization onset temperature (T_x = 612 °C), and the crystallization peak (T_p = 622 °C) were determined. Both glass transition and crystallization peak temperatures agreed with findings of previous works that prepared LAGP glass-ceramics [12,14]. It is noteworthy that quenching of the LAGP melt by splat-cooling between stainless steel plates produced an amorphous LAGP glass, as demonstrated in the diffractogram in Fig. 1b.

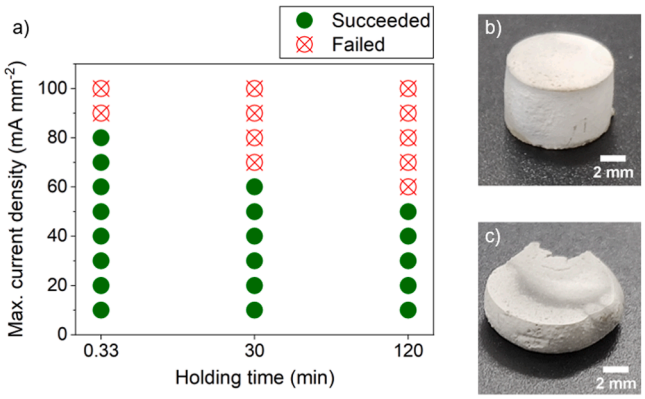

Fig. 2. a) Processing map for *flash sinter-crystallization* with current ramp control of the $Li_{1.5}Al_{0.5}Ge_{1.5}(PO_4)_3$ glass-ceramic. The green circles represent the conditions that succeeded, and the crossed red circles those that failed; b) a picture of a successful *flash sinter-crystallized* sample (120 min holding time and maximum current density of 40 mA mm^{-2}); c) a picture of a failing *flash sinter-crystallized* sample (120 min holding time and maximum current density of 60 mA mm^{-2}).

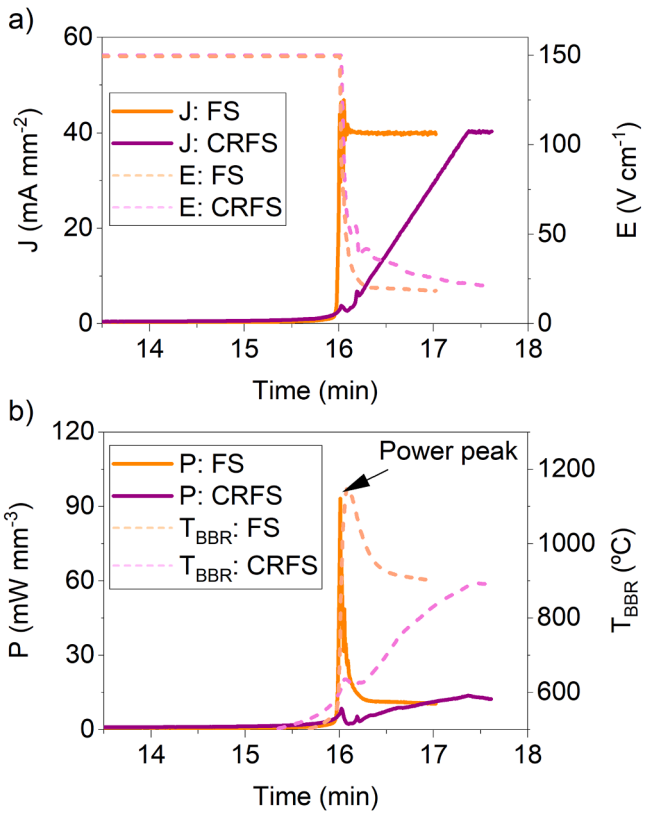

Fig. 3. Evolution over time of a) current density (J) and electric field (E), and b) power density (P) and the estimated temperature (T_{BBR}) calculated using the Black-Body Radiation (BBR) model of the $Li_{1.5}Al_{0.5}Ge_{1.5}(PO_4)_3$ glass-ceramic samples *flash sinter-crystallized* without current ramp control (FS) and with current ramp control (CRFS).

The flash onset temperature was similar for all investigated conditions (468 ± 7 °C). This behavior was expected since we used the same electric field (150 V.cm^{-1}) in all experiments [54] and samples of the same size [51]. Therefore, the flash event was triggered at a furnace temperature approximately 50 °C below T_g. It is worth mentioning that, in some cases, the sample softened and lost its initial geometry. We

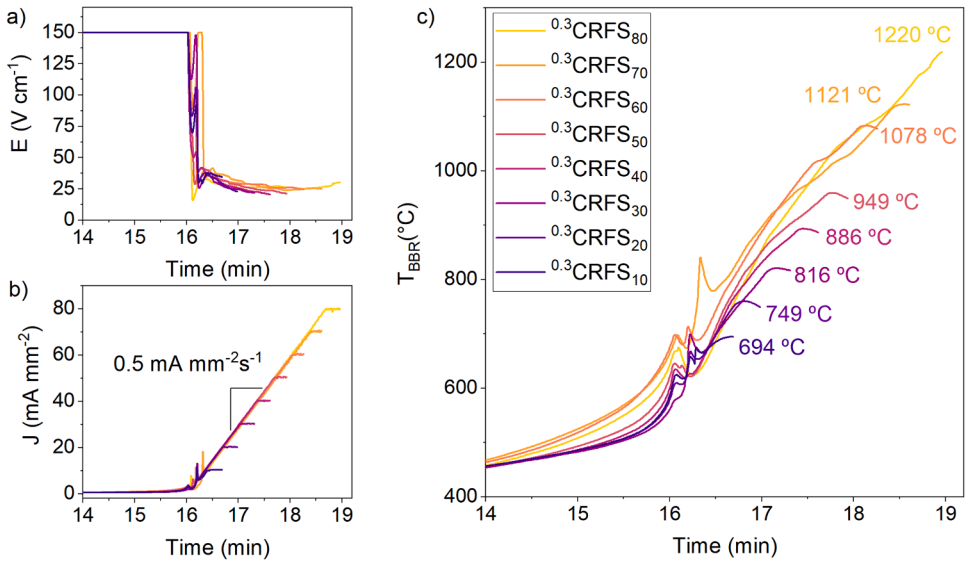

Fig. 4. Evolution over time of a) electric field (E), b) current density (J), and c) the estimated temperature (T_{BBR}) calculated using the BBR model of the $Li_{1.5}Al_{0.5}Ge_{1.5}(PO_4)_3$ (LAGP) glass-ceramic samples *flash sinter-crystallized* with current ramp control (CRFS), 0.3 min holding time after the flash event, and various maximum current densities (from 10 to 80 mA mm^{-2}). Graphs a) and b) share the same color legend shown in graph c). In the graph's c) legend, the CRFS superscript refers to the holding time and the subscript to the maximum pre-set current density (e.g., $^{0.3}CRFS_{40}$ is the sample subjected to 40 mA mm^{-2} for 0.3 min).

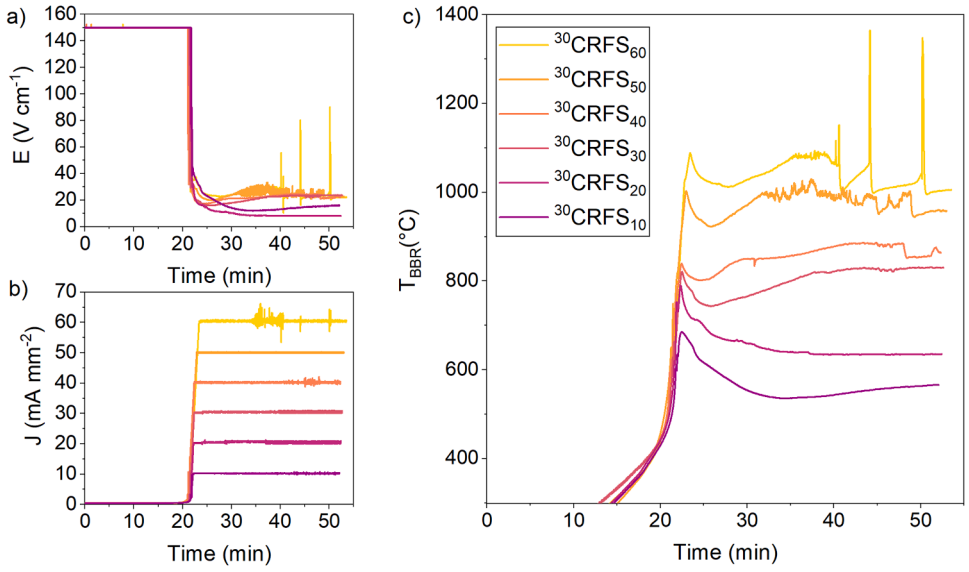

Fig. 5. Evolution over time of a) electric field (E), b) current density (J), and c) the estimated temperature (T_{BBR}) calculated using the BBR model of the $Li_{1.5}Al_{0.5}Ge_{1.5}(PO_4)_3$ (LAGP) glass-ceramic samples *flash sinter-crystallized* with current ramp control (CRFS), with 30 min holding time after the flash event, and various maximum current densities (from 10 to 60 mA mm^{-2}). Graphs a) and b) share the same color legend shown in graph c). In the legend of graph c), the CRFS superscript refers to the holding time and the subscript to the maximum pre-set current density (e.g., $^{30}CRFS_{40}$ is the sample subjected to 40 mA mm^{-2} for 30 min).

treated these cases as failure conditions. Fig. 2a shows a processing map of the studied conditions for the *FSC* of LAGP. An example of a condition that has succeeded is shown in Fig. 2b, while an example of a condition that has failed is presented in Fig. 2c.

Fig. 3 illustrates the current density (J), electric field (E), temperature (estimated by the BBR model - T_{BBR}), and power density (P) vs. time (t) of two samples: one *flash sinter-crystallized* without current ramp control (FS) and one with current ramp control (CRFS). In both experiments, the samples reached the same maximum current density of 40 mA mm^{-2} (Fig. 3a). However, the sample subjected to FS achieved higher temperatures than those prepared by CRFS (Fig. 3b). This higher temperature is related to the delay in the automatic switching from voltage-to-current control of the power supply, which causes a power peak at the flash event. When the current increase is controlled by the software (CRFS), power peak and sample overheating are avoided.

In flash experiments, the sample temperature increases with increasing the current density applied through Joule heating. For instance, Fig. 4c illustrates the temperature (estimated by the BBR model) of samples in which the maximum current density was maintained for 20 s (0.33 min). Even the lowest current density (10 mA mm^{-2}) resulted in a temperature (694 °C) higher than the DSC crystallization peak of LAGP (622 °C). Also, after the flash event, the electric field (Fig. 4a) converges to the same value, regardless of the maximum current density applied (~25 V cm^{-1}).

In the conditions in which the flash event was held for a longer time (30 min and 2 h), variation in the electric field was observed (Fig. 5a). This behavior led to failure at higher current densities (>70 mA mm^{-2}) because the sample temperatures surpassed 1250 °C in some moments, resulting in sample softening and, sometimes, loss of original geometry (Fig. 2b).

Even in condition $^{30}CRFS_{60}$, the sample temperature estimated by the BBR model exceeded 1250 °C for a few seconds when two anomalous electric field peaks occurred (Figs. 5a and 5c). Biesuz et al. [38] reported noisy peaks in the electric field when DC flash sintering soda-lime-silica glass using Pt electrodes. They suggested that these peaks are related to an alkali depletion layer formed close to the anode during DC flash sintering - first reported by McLaren et al. [40]. However, in our case, AC high-frequency (1000 Hz) was used; therefore, it is reasonable to assume that there was no depletion layer. Indeed, we performed EDS in different regions of the sample, and no significant chemical variation between

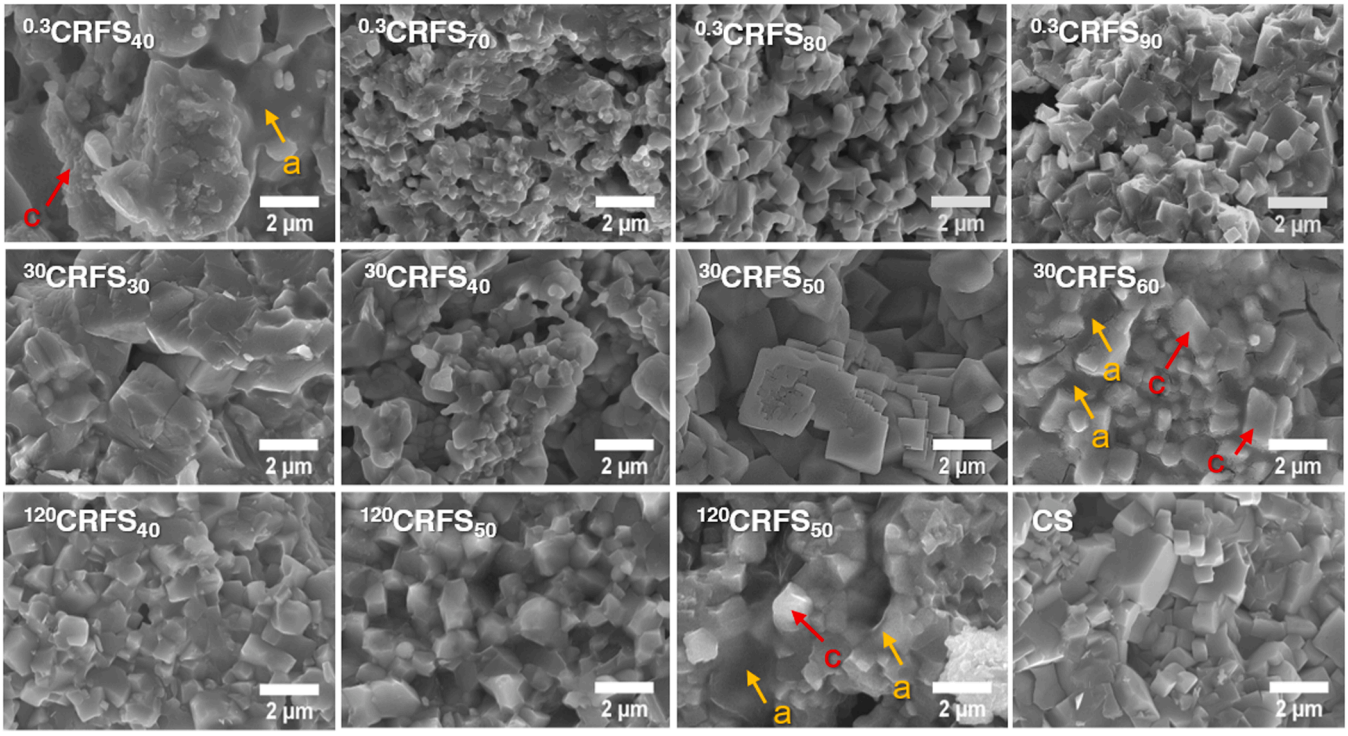

Fig. 6. SEM images of the fractured surface (diametrical fracture) of the $Li_{1.5}Al_{0.5}Ge_{1.5}(PO_4)_3$ (LAGP) glass-ceramic samples *flash sinter-crystallized* with current ramp control (CRFS) and the conventionally sinter-crystallized sample without electric field (CS). The conditions are labeled in each image. The CRFS superscript refers to the holding time, and the subscript to the maximum pre-set current density (e.g., $^{120}CRFS_{40}$ is the sample subjected to 40 mA mm^{-2} for 120 min). The orange arrows (a) indicate amorphous regions, and the red arrows (c) show crystallized regions.

them was verified (see Figs. S6 and S7), nor traces of silver were found. However, since these peaks only appeared after long holding times and high current densities, a possible explanation for their formation is related to oxidation, or even melting, of the silver paste, as previously reported by Frasnelli & Sglavo in a flash sintering experiment conducted with beta-tricalcium phosphate bioceramics using silver paste [55].

The flash sintering curves of samples with 2 h (120 min) holding time were similar to those with 30 min holding time. For further detail, see Fig. S1 in the Supplementary Material.

Fig. 6 depicts the microstructure evolution of samples at different holding times and current densities. The specimens were analyzed in their core and near their flat surfaces, and no significant differences were found between the regions for the same treatment. By increasing the current density limit and the holding time, an increase in the relative density and grain size of the samples was observed. For instance, the grain size of the sample prepared with $^{0.3}CRFS_{70}$ was considerably smaller than those prepared with $^{0.3}CRFS_{80}$ and $^{0.3}CRFS_{90}$. The difference in grain size was even more pronounced when comparing $^{0.3}CRFS_{70}$ with the ones prepared with longer holding time (e.g., $^{30}CRFS_{50}$ and $^{120}CRFS_{50}$). Figs. S2, S3, and S4 in the Supplementary Material show SEM images at different magnifications.

A non-crystallized phase was observed in $^{0.3}CRFS_{40}$ ("a" arrows in Fig. 6), indicating the presence of residual glass for this condition, i.e., the sample has not been fully crystallized. Amorphous-like regions were also found in samples $^{30}CRFS_{60}$ and $^{120}CRFS_{50}$ ("a" arrows in Fig. 6). In these cases, the amorphous phase was not a residual precursor glass since milder treatment conditions (e.g., $^{30}CRFS_{50}$ and $^{120}CRFS_{40}$) resulted in fully crystallized samples. A thermal gradient could be formed at a microscopic level, i.e., between the grains' volume and their boundaries, during the flash processes due to formation of current percolation pathways [56,57]. Therefore, the temperature of some regions in these samples could have exceeded the solidus temperature of LAGP (~1130 °C [13]) and then frozen into a glass on cooling. It is noteworthy that the further increase in the current density of $^{30}CRFS_{60}$ and $^{120}CRFS_{50}$ led to sample softening and loss of original geometry (see Fig. 1).

Presence of the $Li_{1.5}Al_{0.5}Ge_{1.5}(PO_4)_3$ NaSICON phase (International Crystal Structure Database ICSD#263,763 [58]) was confirmed by XRD in all CRFS conditions, regardless of the current densities and holding times used (Fig. 7). A residual glass was detected by XRD as a band at low diffraction angles in samples with 20 s holding time (Figs. 7a and 7b). This amorphous band decreased with increasing the current density until it is no longer detected above 50 mA mm^{-2}, as evidenced in the colormap of Fig. 7a (as well as in Fig. S10). No amorphous phase was detected in samples treated for 30 min (Figs. 7c and 7d) and 120 min (Fig. S9), even for the lowest current density.

Jesus et al. [27] reported the complete crystallization of an amorphous Pechini-derived powder after applying the flash process. In their case, part of the amorphous powder crystallized before the flash event, forming TiO_2 and CuO. Then, during the flash event, $CaCu_3Ti_4O_{12}$ (CCTO) was formed. In our case, the flash event happened below T_g. Thus, no crystallization was achieved before the thermal runaway.

Safanama et al. [59] performed an in situ synchrotron XRD analysis during sintering with concurrent crystallization of a LAGP glass powder without an electric field. They observed that the precursor glass crystallizes before formation of the $LiGe_2(PO_4)_3$ (LGP) rhombohedral phase (Al-poor LAGP phase). Then, with the increase in temperature, Al^{3+} gradually substitutes Ge^{4+} in the LGP structure. This substitution is accompanied by an increase in the concentration of Li^+ in the structure to keep the electroneutrality, and changes in the lattice parameters. Safanama et al. [59] proposed a polynomial equation (Eq. (2)) relating the Al^{3+} content (the $'$ in $Li_{1+x}Al_xGe_{2-x}(PO_4)_3$) and the lattice parameter c:

$$x = 137.951773\ c^3 - 8523.82837\ c^2 + 175,558.931\ c - 1,205,290.72. \quad (2)$$

Using Eq. (2), we estimated x for each studied condition (Table 1 and Fig. 8a). The amount of Al^{3+} entering the LAGP structure tended to

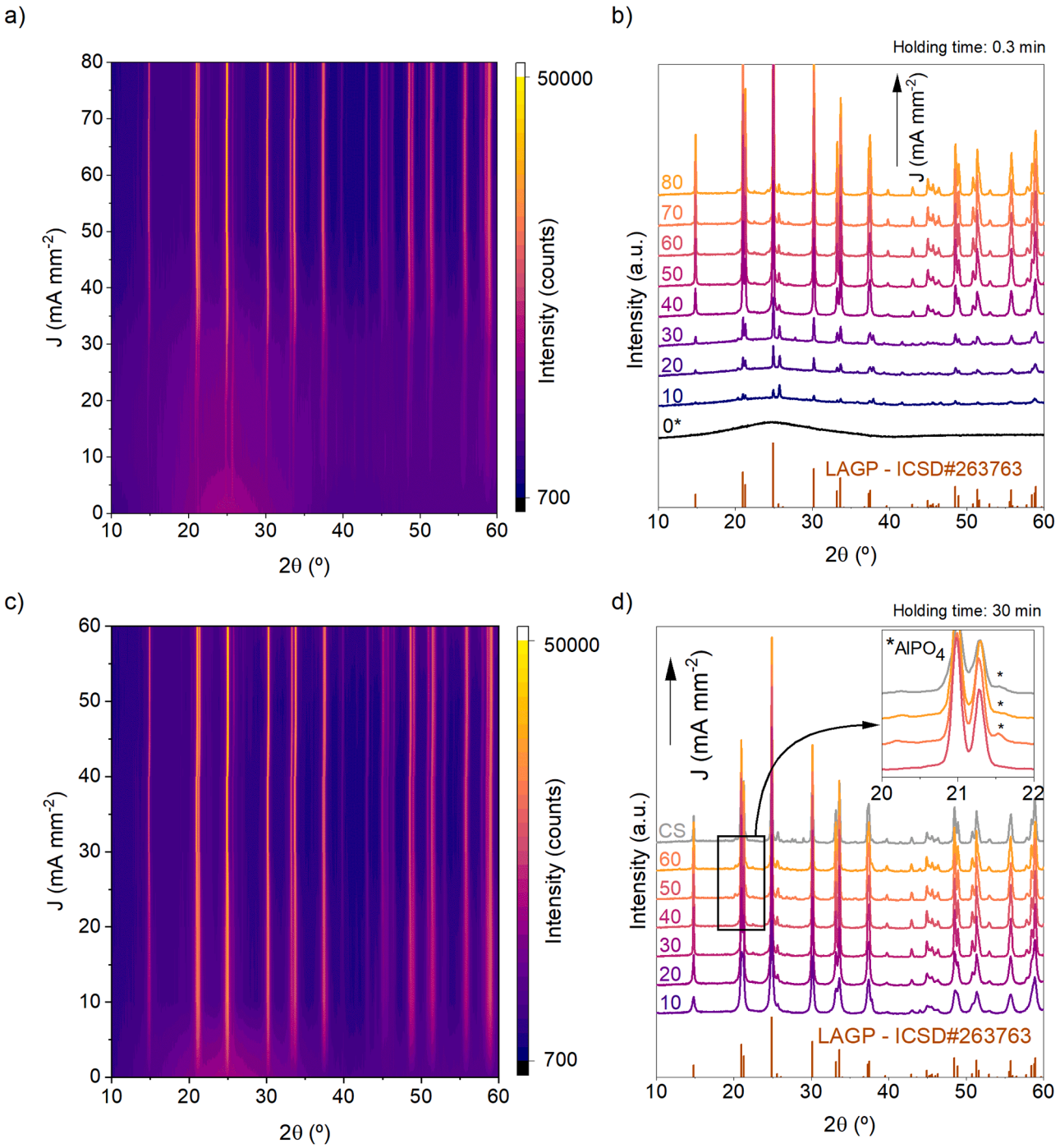

Fig. 7. XRD results for $Li_{1.5}Al_{0.5}Ge_{1.5}(PO_4)_3$ (LAGP) glass-ceramic samples *flash sinter-crystallized* with current ramp control (CRFS) with different current densities (J): at a) and b) 0.33 min holding time, and c) and d) 30 min holding time. 0* corresponds to $J = 0$ mA mm^{-2} (no electric field). CS corresponds to conventional sinter-crystallization at 850 °C for 12 h. Graphs a) and c) are intensity colormaps of the b) and d) plots on the right.

increase with the current density and, consequently, with the increase in temperature, especially for the samples with 30- and 120-min holding times. It is noteworthy that, in some cases (e.g., $^{120}CRFS_{40}$, $^{30}CRFS_{50}$, and $^{30}CRFS_{60}$), x decreased with the formation of an Al-rich secondary phase ($AlPO_4$). The amount of Al incorporated into the structure varied between 0.50 and 0.58. Although the precursor glass was prepared with $x = 0.50$, the 5 mol% excess of Li_2O added to the glass can increase x. Xu et al. [43] demonstrated by nuclear magnetic resonance (NMR) that the excess Li is incorporated into the LAGP structure, affecting its lattice parameters. Thus, it can justify why $x > 0.50$ in most samples.

The amount of Al-substitution in the LAGP structure also affects the peak intensities [15,59]. Thus, the peak intensity ratio (r) between planes (2 $\bar{1}$ 3) and (1 0 4), which corresponds to the peaks position (2θ) of 25.0° and 21.2°, respectively, can also give an estimate of the amount of Al incorporated into the LAGP structure. The Al^{3+} scattering factor is smaller than that of Ge^{4+}, thus r should increase with the Al-substitution (see Fig. S6) [15]. Indeed, higher current densities and longer holding times increased r (Table 1 and Fig. 8b), indicating an increase in the Al incorporation into the LAGP structure.

Regarding the crystallite size, the full width at half maximum (FWHM) of the diffraction peaks decreased with increasing the current density, suggesting that high-current densities promoted larger

Table 1
Amount of secondary phases $AlPO_4$ and $Li_4P_2O_7$, $Li_{1+x}Al_xGe_{2-x}(PO_4)_3$ lattice parameter *c*, estimated amount of Al-substitution (*x*), FWHM of the peak corresponding to plane (2 $\bar{1}$ 3), the ratio (*r*) between the peak intensities of planes (2 $\bar{1}$ 3) and (1 0 4), and the relative density values of the samples for each condition studied. The CRFS superscript refers to the holding time and the subscript to the maximum pre-set current density (e.g., $^{30}CRFS_{40}$ is the sample subjected to 40 mA mm^{-2} for 30 min).

Label	$AlPO_4$ (%)	$Li_4P_2O_7$ (%)	LAGP *c* (Å)	Al-sub (*x*)	FWHM LAGP (2 $\bar{1}$ 3)	Peak ratio (a.u.)	Relative Density (%)
$^{0.3}CRFS_{10}$	–	–	–	–	–	–	54.6
$^{0.3}CRFS_{20}$	–	–	–	–	–	–	57.2
$^{0.3}CRFS_{30}$	–	–	–	–	–	–	63.5
$^{0.3}CRFS_{40}$	–	–	20.650	0.53	0.185	1.46	66.2
$^{0.3}CRFS_{50}$	–	–	20.661	0.55	0.157	1.51	68.4
$^{0.3}CRFS_{60}$	–	–	20.659	0.55	0.131	1.71	72.3
$^{0.3}CRFS_{70}$	–	–	20.660	0.55	0.128	1.77	75.4
$^{0.3}CRFS_{80}$	–	–	20.660	0.55	0.131	1.77	77.8
$^{30}CRFS_{10}$	–	–	20.636	0.50	0.337	1.65	69.8
$^{30}CRFS_{20}$	–	–	20.648	0.52	0.232	1.57	72.8
$^{30}CRFS_{30}$	–	–	20.660	0.55	0.143	1.67	78.2
$^{30}CRFS_{40}$	–	–	20.665	0.56	0.138	1.65	81.5
$^{30}CRFS_{50}$	1.5	2.6	20.653	0.54	0.137	1.91	82.6
$^{30}CRFS_{60}$	1.0	1.5	20.651	0.53	0.134	1.87	82.7
$^{120}CRFS_{10}$	–	–	20.632	0.50	0.245	1.71	69.5
$^{120}CRFS_{20}$	–	2.1	20.647	0.52	0.162	1.61	73.4
$^{120}CRFS_{30}$	–	–	20.656	0.54	0.136	1.63	80.4
$^{120}CRFS_{40}$	0.7	2.4	20.649	0.53	0.126	1.62	82.6
$^{120}CRFS_{50}$	–	1.3	20.670	0.58	0.137	1.89	81.9
CS	0.7	2.2	20.661	0.55	0.162	1.90	80.1

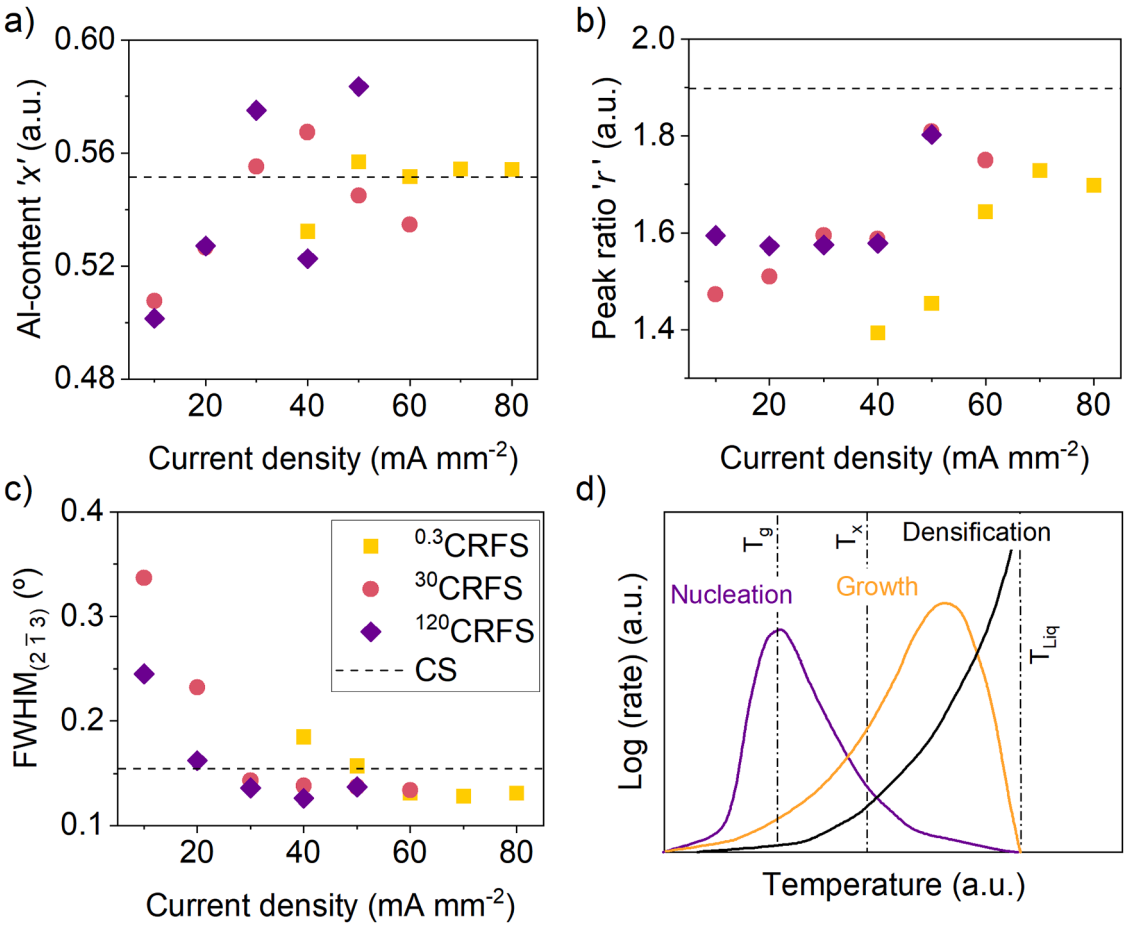

Fig. 8. Influence of maximum current density of flash sinter-crystallization with current ramp on a) estimated content of Al^{3+} (*x*) in the $Li_{1+x}Al_xGe_{2-x}(PO_4)_3$ (LAGP) structure; b) intensity peak ratio between LAGP planes (2 $\bar{1}$ 3) and (1 0 4); c) full width at half maximum (FWHM) of LAGP plane (2 $\bar{1}$ 3); d) schematic illustration of nucleation and growth rates for crystallization and densification as a function of temperature, adapted from Biesuz et al. [60]. Graphs a) and b) share the same color legend presented in graph c).

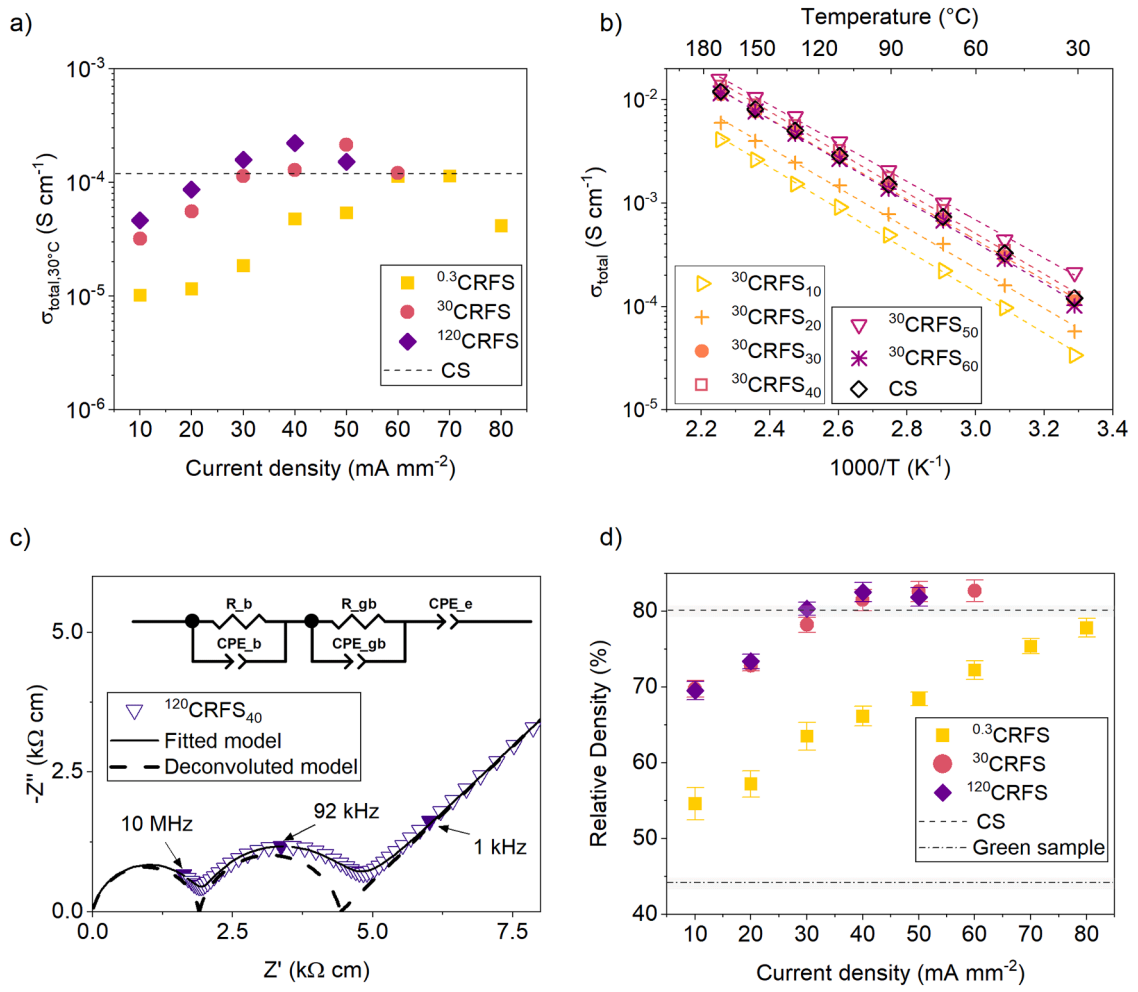

Fig. 9. a) Total ionic conductivity at room temperature of $Li_{1.5}Al_{0.5}Ge_{1.5}(PO_4)_3$ (LAGP) glass-ceramic samples *flash sinter-crystallized* with current ramp control (CRFS) and conventionally sinter-crystallized (CS) samples, b) Arrhenius plot of total (bulk and grain boundary) ionic conductivity of CRFS glass-ceramics with 30 min holding time at the flash state (dashed lines represent the linear fit of the data with $R^2 \geq 0.998$), c) room temperature impedance data (Nyquist plot) for the CRFS sample using 120 min holding time and 40 mA mm^{-2} (fitted using Zview and the represented equivalent electric circuit), and d) relative density of the LAGP glass-ceramic as a function of maximum current density. The CRFS superscript refers to the holding time (e.g., ^{120}CRFS is the sample subjected to 120 min holding time).

crystallite sizes (Fig. 8c and Table 1). In glass-ceramics, the nucleation rate is usually maximum near T_g, and the crystallite growth rate is maximum at ~0.95 T_{Liq} (illustrated in Fig. 8d) [61,62]. Thus, since the heating rate during CRFS is considerably higher than in conventional heating, the samples crystallized at higher temperatures (i.e., with higher current density) should experience less nucleation and more crystallite growth.

A small proportion of secondary phases was observed (see inset in Fig. 7d) in samples with relatively long holding times (30 min and 2 h) and current densities >50 mA mm^{-2}, as well as in the conventionally sintered sample (CS). The proportion of such phases was estimated using the Rietveld refinement (Table 1), whose details can be found in the Supplementary Material (Fig. S5). Previous studies have reported the formation of these secondary phases during conventional heat treatments above 800 °C [59,63,64]. For instance, Safanama et al. [59] observed the formation of a new Al-rich phase (germanium mullite – $Al_{3-x}Ge_xO_{4.5\ +\ x/2}$) when LAGP glass was heated above 820 °C. In our case, two secondary phases ($AlPO_4$ and $Li_4P_2O_7$) were detected in specimens prepared at high current densities and extended holding times (see Table 1). No secondary phase was detected in the samples prepared with a short holding time (0.33 min), even when their temperature exceeded 800 °C.

To analyze the potential of the *flash sinter-crystallized* LAGP as a solid electrolyte, electrical conductivity was measured from room temperature (~30 °C) to 170 °C. The activation energy for ionic conductivity was estimated from the slope of the resulting Arrhenius plot. Fig. 9a summarizes the total electrical conductivity (bulk and grain boundary) at room temperature for each studied condition. Fig. 9b illustrates the influence of temperature on the total conductivity of the samples prepared with a 30 min holding time. We used the Zview software to estimate the total electrical conductivity considering an equivalent circuit of two R//C (resistance in parallel to a Constant Phase Element - CPE) in series. The equivalent circuit used to fit the experimental data and an example of the Nyquist plot (impedance complex plane diagram) of the *flash sinter-crystallized* LAGP ($^{120}CRFS_{40}$) are shown in Fig. 9c. Table S2 (Supplementary Material) contains all the fitted results of the CPE of grain boundary (CPE_gb), bulk (CPE_b), and electrode (CPE_e), as well as the grain boundary (R_gb) and bulk (R_b) resistances. Fig. 9d shows the relative density vs. maximum current density used during the *FSC* process.

For the same current density limit, longer holding times resulted in higher ionic conductivity (Fig. 9a). Furthermore, ionic conductivity increases with increasing current density until reaching a maximum value, and then drops before a further increase (Fig. 9a). Both holding time and current density also affect the densification (Fig. 9d), crystallized fraction (Fig. 7a) and grain size (Fig. 6 and Fig. 8c) of the samples, which can rationalize the behavior observed in the total ionic conductivity. However, the samples with the highest current density for each holding time

Table 2
LAGP bulk and grain boundary activation energies and the pre-exponential factor calculated from Eq. (3) for samples prepared by *flash sinter-crystallization* with current ramp control (CRFS) using 30 min holding time and various maximum current densities (from 10 to 60 mA mm^{-2}), and the sample conventionally sinter-crystallized without electric field (CS). The mathematical error of the activation energies is <0.01 eV.

Sample label	Activation energy (eV)			Log(σ_0) (σ_0: S cm^{-1})		
	Bulk	Grain boundary	Total	Bulk	Grain boundary	Total
$^{30}CRFS_{10}$	0.46	0.31	0.38	3.309	1.402	2.132
$^{30}CRFS_{20}$	0.46	0.34	0.39	3.600	2.006	2.190
$^{30}CRFS_{30}$	0.46	0.34	0.37	3.821	2.100	2.505
$^{30}CRFS_{40}$	0.46	0.34	0.39	4.045	2.257	2.627
$^{30}CRFS_{50}$	0.47	0.34	0.39	3.447	2.254	2.387
$^{30}CRFS_{60}$	0.42	0.33	0.38	3.571	2.050	2.573
CS	0.45	0.32	0.39	3.726	1.935	2.510

($^{120}CRFS_{50}$, $^{30}CRFS_{60}$, and $^{0.3}CRFS_{80}$) showed a decrease in their ionic conductivity, which is not related to their apparent density and grain size. We suggest that, in these cases, the decrease in ionic conductivity can be explained by a local melting of the material, as previously discussed (see Figs. 6 and S2, S3, and S4). It is worth noticing that the ionic conductivity at room temperature of the glassy phase is several orders of magnitude lower than that of the crystallized phase (10^{-9} S cm^{-1} [13] and 10^{-4} S cm^{-1}, respectively).

Therefore, samples with an intermediate current density and longer holding times (e.g., $^{120}CRFS_{40}$ and $^{30}CRFS_{50}$) achieved higher ionic conductivity because crystal growth was favored and the melting point was avoided, resulting in larger grain sizes and more homogeneous microstructures. In the case of a shorter holding time (20 s), higher current densities favored ionic conductivity. This behavior can be explained by the increase in crystallinity and apparent density.

Table 2 presents the activation energy (E_a) and pre-exponential factor (σ_0) values of the ionic conductivity for the grain (bulk) and grain boundaries calculated for samples with 30 min holding time and the conventionally heated sample by Eq. (3):

$$\sigma_{total} = \sigma_0 e^{\left(-\frac{Ea}{kT}\right)}, \quad (3)$$

where σ_{total} is the total ionic conductivity, k is the Boltzmann constant, and T is the absolute temperature.

The total activation energy (0.38 ± 0.01 eV) was similar for all conditions, even for the sample prepared by conventional heating. This activation energy is consistent with Li-ion conduction for the same material described in detail in refs. [65,66] and other experimental results [14,67].

4. Conclusion

We proposed *Flash Sinter-crystallization*, a new method derived from flash sintering to concurrently sinter and crystallize LAGP glasses to obtain glass-ceramics in a few seconds using an electric field and Joule heating as the primary energy sources. A processing map varying the maximum current density and the processing holding time was shown for the LAGP-0.05Li_2O system. The results showed that the electric current density and its holding time influence the microstructure, crystallization kinetics, and ionic conductivity of the material. In summary, a holding time of 30 min and a current density of 50 mA mm^{-2} were optimal to achieve high ionic conductivity (2.26 10^{-4} S cm^{-1}), which was higher than that of the sample conventionally heated for 12 h (1.36 10^{-4} S cm^{-1}).

Declaration of Competing Interest

The authors declare that they have no known competing financial interests or personal relationships that could have appeared to influence the work reported in this paper.

Acknowledgments

This work was supported by the São Paulo Research Foundation (FAPESP) [grant numbers: 2021/06509–9, 2021/11552–0, 2021/12412–8, 2013/07793–6, and 2019/14677–9]. This study was financed in part by the Coordenação de Aperfeiçoamento de Pessoal de Nível Superior - Brasil (CAPES) - Finance Code 001. João Vitor Campos thanks Dr. Lilian M. Jesus and Dr. Bola Yoon for their valuable critical comments on the discussion section of this manuscript.

Supplementary materials

Supplementary material associated with this article can be found, in the online version, at doi:10.1016/j.actamat.2022.118593.

References

[1] X. He, Y. Zhu, Y. Mo, Origin of fast ion diffusion in superionic conductors, Nat. Commun. 8 (2017) 1–7, https://doi.org/10.1038/ncomms15893.
[2] Y. Zhu, X. He, Y. Mo, First principles study on electrochemical and chemical stability of solid electrolyte–electrode interfaces in all-solid-state Li-ion batteries, J. Mater. Chem. A. 4 (2016) 3253–3266, https://doi.org/10.1039/C5TA08574H.
[3] Y. Tian, G. Zeng, A. Rutt, T. Shi, H. Kim, J. Wang, J. Koettgen, Y. Sun, B. Ouyang, T. Chen, Z. Lun, Z. Rong, K. Persson, G. Ceder, Promises and Challenges of Next-Generation "beyond Li-ion" Batteries for Electric Vehicles and Grid Decarbonization, Chem. Rev. 121 (2021) 1623–1669, https://doi.org/10.1021/acs.chemrev.0c00767.
[4] K. Takada, Progress and prospective of solid-state lithium batteries, Acta Mater. 61 (2013) 759–770, https://doi.org/10.1016/j.actamat.2012.10.034.
[5] E. Zhao, F. Ma, Y. Guo, Y. Jin, Stable LATP/LAGP double-layer solid electrolyte prepared via a simple dry-pressing method for solid state lithium ion batteries, RSC Adv. 6 (2016) 92579–92585, https://doi.org/10.1039/C6RA19415J.
[6] J.A. Dias, S.H. Santagneli, Y. Messaddeq, Methods for Lithium Ion NASICON Preparation: From Solid-State Synthesis to Highly Conductive Glass-Ceramics, J. Phys. Chem. C. 124 (2020) 26518–26539, https://doi.org/10.1021/acs.jpcc.0c07385.
[7] R. DeWees, H. Wang, Synthesis and Properties of NaSICON-type LATP and LAGP Solid Electrolytes, ChemSusChem 12 (2019) 3713–3725, https://doi.org/10.1002/cssc.201900725.
[8] C.R. Mariappan, C. Yada, F. Rosciano, B. Roling, Correlation between micro-structural properties and ionic conductivity of Li1.5Al0.5Ge1.5(PO4)3 ceramics, J. Power Sources. 196 (2011) 6456–6464, https://doi.org/10.1016/j.jpowsour.2011.03.065.
[9] M. Zhang, Z. Huang, J. Cheng, O. Yamamoto, N. Imanishi, B. Chi, J. Pu, J. Li, Solid state lithium ionic conducting thin film Li1.4Al 0.4Ge1.6(PO4)3 prepared by tape casting, J. Alloys Compd. 590 (2014) 147–152, https://doi.org/10.1016/j.jallcom.2013.12.100.
[10] M. Zhang, K. Takahashi, N. Imanishi, Y. Takeda, O. Yamamoto, B. Chi, J. Pu, J. Li, Preparation and Electrochemical Properties of Li 1+x Al x Ge 2-x (PO 4) 3 Synthesized by a Sol-Gel Method, J. Electrochem. Soc. 159 (2012) A1114–A1119, https://doi.org/10.1149/2.080207jes.
[11] M. Kotobuki, M. Koishi, Preparation of Li1.5Al0.5Ge1.5(PO4)3 solid electrolytes via the co-precipitation method, J. Asian Ceram. Soc. 7 (2019) 551–557, https://doi.org/10.1080/21870764.2019.1693680.
[12] A.M. Rodrigues, J.L. Narváez-Semanate, A.A. Cabral, A.C.M. Rodrigues, Determination of crystallization kinetics parameters of a Li1.5Al0.5Ge1.5(PO4)3 (LAGP) glass by differential scanning calorimetry, Mater. Res. 16 (2013) 811–816, https://doi.org/10.1590/S1516-14392013005000055.
[13] A.M. Cruz, E.B. Ferreira, A.C.M. Rodrigues, Controlled crystallization and ionic conductivity of a nanostructured LiAlGePO4 glass–ceramic, J. Non. Cryst. Solids. 355 (2009) 2295–2301, https://doi.org/10.1016/j.jnoncrysol.2009.07.012.
[14] C. Schröder, J. Ren, A.C.M. Rodrigues, H. Eckert, Glass-to-Crystal Transition in Li 1 + x Al x Ge 2– x (PO 4) 3 : Structural Aspects Studied by Solid State NMR, J. Phys. Chem. C. 118 (2014) 9400–9411, https://doi.org/10.1021/jp502265h.
[15] J. Fu, Fast Li+ ion conducting glass-ceramics in the system Li2O-Al2O3-GeO2-P2O5, Solid State Ionics 104 (1997) 191–194, https://doi.org/10.1016/s0167-2738(97)00434-7.
[16] E.D. Zanotto, A bright future for glass-ceramics, Am. Ceram. Soc. Bull. 89 (2010) 27.
[17] J. Deubener, M. Allix, M.J. Davis, A. Duran, T. Höche, T. Honma, T. Komatsu, S. Krüger, I. Mitra, R. Müller, S. Nakane, M.J. Pascual, J.W.P. Schmelzer, E. D. Zanotto, S. Zhou, Updated definition of glass-ceramics, J. Non. Cryst. Solids. 501 (2018) 3–10, https://doi.org/10.1016/j.jnoncrysol.2018.01.033.
[18] M. Cologna, B. Rashkova, R. Raj, Flash Sintering of Nanograin Zirconia in <5 s at 850°C, J. Am. Ceram. Soc. 93 (2010) 3556–3559, https://doi.org/10.1111/j.1551-2916.2010.04089.x.

[19] J. Liu, X. Li, X. Wang, R. Huang, Z. Jia, Alternating current field flash sintering 99% relative density ZnO ceramics at room temperature, Scr. Mater. 176 (2020) 28–31, https://doi.org/10.1016/j.scriptamat.2019.09.026.

[20] J. Nie, Y. Zhang, J.M. Chan, R. Huang, J. Luo, Water-assisted flash sintering: Flashing ZnO at room temperature to achieve ~ 98% density in seconds, Scr. Mater. 142 (2018) 79–82, https://doi.org/10.1016/j.scriptamat.2017.08.032.

[21] A. Gaur, V.M. Sglavo, Densification of La0.6Sr0.4Co0.2Fe 0.8O3 ceramic by flash sintering at temperature less than 100°C, J. Mater. Sci. 49 (2014) 6321–6332, https://doi.org/10.1007/s10853-014-8357-2.

[22] X. Wang, Y. Zhu, R. Huang, H. Mei, Z. Jia, Flash sintering of ZnO ceramics at 50 °C under an AC field, Ceram. Int. 45 (2019) 24909–24913, https://doi.org/10.1016/j.ceramint.2019.08.142.

[23] S. Grasso, Y. Sakka, N. Rendtorff, C. Hu, G. Maizza, H. Borodianska, O. Vasylkiv, Modeling of the temperature distribution of flash sintered zirconia, J. Ceram. Soc. Japan. 119 (2011) 144–146, https://doi.org/10.2109/jcersj2.119.144.

[24] I.R. Lavagnini, J.V. Campos, J.A. Ferreira, E.M.J.A. Pallone, Microstructural evolution of 3YSZ flash-sintered with current ramp control, J. Am. Ceram. Soc. 103 (2020) 3493–3499, https://doi.org/10.1111/jace.17037.

[25] H. Charalambous, S.K. Jha, K.H. Christian, R.T. Lay, T. Tsakalakos, Flash Sintering using Controlled Current Ramp, J. Eur. Ceram. Soc. 38 (2018) 3689–3693, https://doi.org/10.1016/j.jeurceramsoc.2018.04.003.

[26] M.K. Punith Kumar, D. Yadav, J.M. Lebrun, R. Raj, Flash sintering with current rate: A different approach, J. Am. Ceram. Soc. 102 (2018) 1–13, https://doi.org/10.1111/jace.16037.

[27] L.M. Jesus, R.S. Silva, R. Raj, J.C. M'Peko, Electric field-assisted ultrafast synthesis of nanopowders: a novel and cost-efficient approach, RSC Adv 6 (2016) 107208–107213, https://doi.org/10.1039/C6RA18734J.

[28] M. Biesuz, V.M. Sglavo, Beyond flash sintering: How the flash event could change ceramics and glass processing, Scr. Mater. 187 (2020) 49–56, https://doi.org/10.1016/j.scriptamat.2020.05.065.

[29] B. Yoon, V. Avila, R. Raj, L.M. Jesus, Reactive flash sintering of the entropy-stabilized oxide Mg0.2Ni0.2Co0.2Cu0.2Zn0.2O, Scr. Mater 181 (2020) 48–52, https://doi.org/10.1016/j.scriptamat.2020.02.006.

[30] V. Avila, B. Yoon, R.R. Ingraci Neto, R.S. Silva, S. Ghose, R. Raj, L.M. Jesus, Reactive flash sintering of the complex oxide Li0.5La0.5TiO3 starting from an amorphous precursor powder, Scr. Mater. 176 (2020) 78–82, https://doi.org/10.1016/j.scriptamat.2019.09.037.

[31] V. Avila, B. Yoon, S. Ghose, R. Raj, L.M. Jesus, Phase evolution during reactive flash sintering of Li6.25Al0.25La3Zr2O12 starting from a chemically prepared powder, J. Eur. Ceram. Soc. 41 (2021) 4552–4557, https://doi.org/10.1016/j.jeurceramsoc.2021.02.054.

[32] B. Yoon, D. Yadav, S. Ghose, P. Sarin, R. Raj, On the synchronicity of flash sintering and phase transformation, J. Am. Ceram. Soc. 102 (2019) 3110–3116, https://doi.org/10.1111/jace.16335.

[33] B. Yoon, V. Avila, R. Kathiria, L.M. Jesus, Effects of powder dispersion on reactive flash sintering of 8 mol% yttria-stabilized zirconia and MgAl2O4 composites, Scr. Mater. 189 (2020) 117–121, https://doi.org/10.1016/j.scriptamat.2020.08.009.

[34] R.R. Ingraci Neto, E. Kardoulaki, J.A. Valdez, The influence of the processing parameters on the reactive flash sintering of ZrO 2 -CeO 2, J. Am. Ceram. Soc. (2022) 1–12, https://doi.org/10.1111/jace.18426.

[35] B. Yoon, V. Avila, I.R. Lavagnini, J.V. Campos, L.M. Jesus, Reactive flash sintering of ceramics: a review, Adv. Eng. Mater. (2022), https://doi.org/10.1002/adem.202200731.

[36] F. Liu, B. Bai, L. Cheng, C. Xu, Rapid synthesis of Li 4 Ti 5 O 12 as lithium-ion battery anode by reactive flash sintering, J. Am. Ceram. Soc. 105 (2022) 419–427, https://doi.org/10.1111/jace.18086.

[37] M.O. Prado, M. Biesuz, M. Frasnelli, F.E. Benedetto, V.M. Sglavo, Viscous flow flash sintering of porous silica glass, J. Non. Cryst. Solids. 476 (2017) 60–66, https://doi.org/10.1016/j.jnoncrysol.2017.09.024.

[38] M. Biesuz, M. Cipriani, V.M. Sglavo, G.D. Sorarù, Electrode-dependent Joule heating in soda lime silicate glass during flash processes, Scr. Mater. 182 (2020) 94–98, https://doi.org/10.1016/j.scriptamat.2020.03.005.

[39] L. Pinter, M. Biesuz, V.M. Sglavo, T. Saunders, J. Binner, M. Reece, S. Grasso, DC-electro softening in soda lime silicate glass: An electro-thermal analysis, Scr. Mater. 151 (2018) 14–18, https://doi.org/10.1016/j.scriptamat.2018.03.028.

[40] C. Mclaren, W. Heffner, R. Tessarollo, R. Raj, H. Jain, Electric field-induced softening of alkali silicate glasses, 184101 (2015) 1–6. 10.1063/1.4934945.

[41] C.T. McLaren, C. Kopatz, N.J. Smith, H. Jain, Development of highly inhomogeneous temperature profile within electrically heated alkali silicate glasses, Sci. Rep. 9 (2019) 2805, https://doi.org/10.1038/s41598-019-39431-8.

[42] M. Biesuz, M. Bortolotti, F. Tessarolo, R. Canteri, P. Giopato, G. Nollo, A. Chiappini, M. Vilémová, V.M. Sglavo, G.D. Sorarù, Solid-state field-assisted ion exchange of Ag in lithium aluminum silicate glass-ceramics: A superfast processing route toward stronger materials with antimicrobial properties, J. Eur. Ceram. Soc. 42 (2022) 1750–1761, https://doi.org/10.1016/j.jeurceramsoc.2021.11.035.

[43] X. Xu, Z. Wen, X. Wu, X. Yang, Z. Gu, Lithium Ion-Conducting Glass-Ceramics of Li 1.5 Al 0.5 Ge 1.5 (PO 4) 3 -xLi 2 O (x=0.0-0.20) with Good Electrical and Electrochemical Properties, J. Am. Ceram. Soc. 90 (2007) 2802–2806, https://doi.org/10.1111/j.1551-2916.2007.01827.x.

[44] L.B. Caliman, R. Bouchet, D. Gouvea, P. Soudant, M.C. Steil, Flash sintering of ionic conductors: The need of a reversible electrochemical reaction, J. Eur. Ceram. Soc. 36 (2016) 1253–1260, https://doi.org/10.1016/j.jeurceramsoc.2015.12.005.

[45] M. Lachal, H. El Khal, D. Bouvard, J. Chaix, R. Bouchet, M.C. Steil, Flash sintering of cationic conductive ceramics: A way to build multilayer systems, J. Am. Ceram. Soc. 104 (2021) 3845–3854, https://doi.org/10.1111/jace.17787.

[46] J.V. Campos, I.R. Lavagnini, R.V. de Sousa, J.A. Ferreira, E.M.J.A. Pallone, Development of an instrumented and automated flash sintering setup for enhanced process monitoring and parameter control, J. Eur. Ceram. Soc. 39 (2019) 531–538, https://doi.org/10.1016/j.jeurceramsoc.2018.09.002.

[47] J.V. Campos, I.R. Lavagnini, V. Avila, B. Yoon, S. Ghose, R. Raj, E.M.J.A. Pallone, L. M. Jesus, On the Arrhenius-like behavior of conductivity during flash sintering of 3 mol% yttria stabilized zirconia ceramics, Scr. Mater. 203 (2021), 114093, https://doi.org/10.1016/j.scriptamat.2021.114093.

[48] P. Kumar M K, D. Yadav, J. Lebrun, R. Raj, Flash sintering with current rate: A different approach, J. Am. Ceram. Soc. 102 (2019) 823–835, https://doi.org/10.1111/jace.16037.

[49] I.R. Lavagnini, J.V. Campos, E.M.J.A. Pallone, Microstructure evaluation of 3YSZ sintered by Two-Step Flash Sintering, Ceram. Int. 47 (2021) 21618–21624, https://doi.org/10.1016/j.ceramint.2021.04.174.

[50] M. Rohde, Y. Cui, C. Ziebert, H.J. Seifert, Thermophysical Properties of Lithium Aluminum Germanium Phosphate with Different Compositions, Int. J. Thermophys. 41 (2020) 31, https://doi.org/10.1007/s10765-020-2607-0.

[51] J.V. Campos, I.R. Lavagnini, J.G. Pereira da Silva, J.A. Ferreira, R.V. Sousa, R. Mücke, O. Guillon, E.M.J.A. Pallone, Flash sintering scaling-up challenges: Influence of the sample size on the microstructure and onset temperature of the flash event, Scr. Mater. 186 (2020) 1–5, https://doi.org/10.1016/j.scriptamat.2020.04.022.

[52] C.A. Grimley, S. Funni, C. Green, E.C. Dickey, A thermal perspective of flash sintering: The effect of AC current ramp rate on microstructure evolution, J. Eur. Ceram. Soc. 41 (2021) 2807–2817, https://doi.org/10.1016/j.jeurceramsoc.2020.11.040.

[53] B.H. Toby, R.B. Von Dreele, GSAS-II : the genesis of a modern open-source all purpose crystallography software package, J. Appl. Crystallogr. 46 (2013) 544–549, https://doi.org/10.1107/S0021889813003531.

[54] J.S.C. Francis, R. Raj, Influence of the Field and the Current Limit on Flash Sintering at Isothermal Furnace Temperatures, J. Am. Ceram. Soc. 96 (2013) 2754–2758, https://doi.org/10.1111/jace.12472.

[55] M. Frasnelli, V.M. Sglavo, Flash sintering of tricalcium phosphate (TCP) bioceramics, J. Eur. Ceram. Soc. 38 (2018) 279–285, https://doi.org/10.1016/j.jeurceramsoc.2017.08.004.

[56] R. Serrazina, P.M. Vilarinho, A.M.O.R. Senos, L. Pereira, I.M. Reaney, J.S. Dean, Modelling the particle contact influence on the Joule heating and temperature distribution during FLASH sintering, J. Eur. Ceram. Soc. 40 (2020) 1205–1211, https://doi.org/10.1016/j.jeurceramsoc.2019.12.015.

[57] K.S.N. Vikrant, H. Wang, A. Jana, H. Wang, R.E. García, Flash sintering incubation kinetics, Npj Comput. Mater. 6 (2020) 1–8, https://doi.org/10.1038/s41524-020-00359-7.

[58] M. Weiss, D.A. Weber, A. Senyshyn, J. Janek, W.G. Zeier, Correlating Transport and Structural Properties in Li 1+ x Al x Ge 2– x (PO 4) 3 (LAGP) Prepared from Aqueous Solution, ACS Appl. Mater. Interfaces. 10 (2018) 10935–10944, https://doi.org/10.1021/acsami.8b00842.

[59] D. Safanama, N. Sharma, R.P. Rao, H.E.A. Brand, S. Adams, Structural evolution of NASICON-type Li 1+x Al x Ge 2−x (PO 4) 3 using in situ synchrotron X-ray powder diffraction, J. Mater. Chem. A. 4 (2016) 7718–7726, https://doi.org/10.1039/C6TA00402D.

[60] M. Biesuz, V.M. Sglavo, Flash sintering of ceramics, J. Eur. Ceram. Soc. 39 (2019) 115–143, https://doi.org/10.1016/j.jeurceramsoc.2018.08.048.

[61] J. Jiusti, E.D. Zanotto, D.R. Cassar, M.R.B. Andreeta, Viscosity and liquidus-based predictor of glass-forming ability of oxide glasses, J. Am. Ceram. Soc. 103 (2020) 921–932, https://doi.org/10.1111/jace.16732.

[62] J.W.P. Schmelzer, A.S. Abyzov, V.M. Fokin, C. Schick, E.D. Zanotto, Crystallization of glass-forming liquids: Maxima of nucleation, growth, and overall crystallization rates, J. Non. Cryst. Solids. 429 (2015) 24–32, https://doi.org/10.1016/j.jnoncrysol.2015.08.023.

[63] V.M. Zallocco, J.M. Freitas, N. Bocchi, A.C.M. Rodrigues, Electrochemical stability of a NASICON solid electrolyte from the lithium aluminum germanium phosphate (LAGP) series, Solid State Ionics 378 (2022), 115888, https://doi.org/10.1016/j.ssi.2022.115888.

[64] S.V. Pershina, B.D. Antonov, A.S. Farlenkov, E.G. Vovkotrub, Glass-ceramics in Li1+xAlxGe2-x(PO4)3 system: The effect of Al2O3 addition on microstructure, structure and electrical properties, J. Alloys Compd. 835 (2020), 155281, https://doi.org/10.1016/j.jallcom.2020.155281.

[65] P.H. Kuo, J. Du, Lithium Ion Diffusion Mechanism and Associated Defect Behaviors in Crystalline Li 1+ x Al x Ge 2– x (PO 4) 3 Solid-State Electrolytes, J. Phys. Chem. C. 123 (2019) 27385–27398, https://doi.org/10.1021/acs.jpcc.9b08390.

[66] A. Vyalikh, M. Schikora, K.P. Seipel, M. Weigler, M. Zschornak, F. Meutzner, W. Münchgesang, T. Nestler, V. Vizgalov, D. Itkis, A.F. Privalov, M. Vogel, Di. C. Meyer, NMR studies of Li mobility in NASICON-type glass-ceramic ionic conductors with optimized microstructure, J. Mater. Chem. A. 7 (2019) 13968–13977, https://doi.org/10.1039/C8TA11686E.

[67] K. Arbi, W. Bucheli, R. Jiménez, J. Sanz, High lithium ion conducting solid electrolytes based on NASICON Li 1+x Al x M 2−x (PO 4) 3 materials (M = Ti, Ge and 0 ≤ x ≤ 0.5), J. Eur. Ceram. Soc. 35 (2015) 1477–1484, https://doi.org/10.1016/j.jeurceramsoc.2014.11.023.